

Quantifying mechanical forces during vertebrate morphogenesis

Eirini Maniou

Developmental Biology and Cancer, UCL GOS Institute of Child Health, London UK

Silvia Todros

Department of Industrial Engineering, University of Padova, Padova, Italy

Anna Urciuolo

Department of Industrial Engineering, University of Padova, Padova, Italy; Fondazione Istituto di Ricerca Pediatrica, Città della Speranza, Padova, Italy <https://orcid.org/0000-0001-7571-9747>

Dale Moulding

Developmental Biology and Cancer, UCL GOS Institute of Child Health, London UK

<https://orcid.org/0000-0002-1431-7047>

Michael Magnusson

Developmental Biology and Cancer, UCL GOS Institute of Child Health, London UK

<https://orcid.org/0000-0003-3054-9806>

Monica Giomo

Department of Industrial Engineering, University of Padova, Padova, Italy; Veneto Institute of Molecular Medicine, Padova, Italy <https://orcid.org/0000-0002-7690-1054>

Piero G. Pavan

Department of Industrial Engineering, University of Padova, Padova, Italy; Fondazione Istituto di Ricerca Pediatrica, Città della Speranza, Padova, Italy

Gabriel L. Galea (✉ g.galea@ucl.ac.uk)

Developmental Biology and Cancer, UCL GOS Institute of Child Health, London UK

Nicola Elvassore (✉ n.elvassore@ucl.ac.uk)

Developmental Biology and Cancer, UCL GOS Institute of Child Health, London UK; Department of Industrial Engineering, University of Padova, Padova, Italy; Veneto Institute of Molecular Medicine, Padova, Italy

Article

Keywords: Force-sensor, embryo, biomechanics, neural tube, intravital bioprinting

Posted Date: February 17th, 2022

DOI: <https://doi.org/10.21203/rs.3.rs-1095730/v1>

License:  This work is licensed under a Creative Commons Attribution 4.0 International License.

[Read Full License](#)

1 **Quantifying mechanical forces during vertebrate morphogenesis**

2

3 Eirini Maniou¹, Silvia Todros², Anna Urciuolo^{2,3}, Dale Moulding¹, Michael Magnusson¹, Monica
4 Giomo^{2,4}, Piero G. Pavan^{2,3}, Gabriel L Galea^{1,*}, Nicola Elvassore^{1,2,4*}

5

6 1. Developmental Biology and Cancer, UCL GOS Institute of Child Health, London UK

7 2. Department of Industrial Engineering, University of Padova, Padova, Italy

8 3. Fondazione Istituto di Ricerca Pediatrica, Città della Speranza, Padova, Italy

9 4. Veneto Institute of Molecular Medicine, Padova, Italy

10

11 * These authors contributed equally. Order determined by coin toss. Corresponding to:
12 g.galea@ucl.ac.uk; n.elvassore@ucl.ac.uk

13

14

15 **Key words:**

16 Force-sensor, embryo, biomechanics, neural tube, intravital bioprinting

17

18 **Abstract**

19 Morphogenesis, the establishment of rudimentary organ structures, requires embryonic cells to
20 generate forces and perform mechanical work to shape their tissues. Incorrect functioning of these
21 force fields can lead to congenital malformations including neural tube defects. The understanding
22 of these dynamic processes requires quantification and profiling of three-dimensional mechanics
23 during evolving vertebrate morphogenesis, which is not tractable with current technology. We
24 fabricated elastic spring-like force sensors with micron-level resolution directly into specific three-
25 dimensional domains of the closing neural tubes of growing chicken embryos through intravital
26 three-dimensional bioprinting. Integration of calibrated sensor readouts with computational
27 mechanical modelling allows direct quantification of forces and work performed by embryonic
28 tissues. The two halves of the closing neural tube at the embryonic midline reach over a hundred
29 nano-Newton compression during neural fold apposition. Unexpectedly, diminishing pro-closure
30 force by pharmacologically inhibiting Rho-associated kinase reveals active anti-closure forces
31 which must depend on alternative mechanisms or tissue properties, and which progressively widen
32 the neural tube. Pro-morphogenetic forces must therefore overcome anti-morphogenetic forces to
33 achieve neural tube closure.

34 **Introduction**

35 Morphogenesis is the quintessentially biomechanical process by which embryonic cells change
36 their tissue's shape, establishing the form necessary for subsequent organ function. Intricate
37 dynamics between multiscale force fields and biochemical factors acting on heterogenous cell
38 populations impose evolving geometrical constraints and allow developing embryos to robustly
39 self-organise organ rudiments (1, 2). Failures of morphogenesis and uncoupling between "passive"
40 mechanical properties and "active" force generation, associated with genetic and environmental
41 factors, produce congenital anomalies which remain a major cause of infant mortality globally.
42 Across Europe, nearly 27 per 1,000 births are affected by a congenital anomaly (3) and neural tube
43 defects (NTDs) remain among the most common and severe congenital malformations (4). These
44 defects are caused by failure to close the embryonic neural tube, a biophysical process which has
45 long served as a clinically-relevant paradigm of morphogenesis (5).

46 The neural tube is the embryonic precursor of the vertebrate central nervous system. It
47 mechanically closes through dorsal bending and medial apposition of the initially flat
48 neuroepithelium into a continuous tube. Closure is a complex, coordinated, dynamic process in
49 which active multi-scale cell-generated forces exceed residual tissue stresses to produce tubular
50 morphogenesis (6-9). Genetic or teratogenic disruptions of neural tube closure biomechanics can
51 cause neural tube defects (10, 11). Although essential, the analysis of morphogenetic forces
52 generated during vertebrate neural tube closure has not yet been possible. State of the art force-
53 inference techniques, mainly based on destructive ablation or cantilever probing only allow partial
54 quantification of NT closure mechanics (12, 13) and they are limited small temporal windows and
55 small tissue landscape. In this view, some techniques were recently developed, including the use
56 of using lipid droplets incorporated in developing zebrafish embryos, to provide fundamental
57 insights into the fluidization of maturing tissue (14), however, they do not enable directional force
58 quantification.

59 We envisioned designing force-sensor technology to quantify the biomechanics of neural tube
60 closure and to provide a temporal profile of evolving forces and mechanical work generated in
61 living vertebrate embryos. This aim imposes pre-determined requirements. The force sensor
62 technology must be compatible with embryo development to provide mechanical readouts over
63 developmentally relevant timeframes of several hours. For example, the chick rhombocervical
64 neuropore (RNP) closes over approximately five hours (15). Physical force sensors must have
65 compliant elastic properties sensitive to imposition of forces in the nano-Newton to micro-Newton
66 range. Achieving elastic compliance requires control over sensor shape, bulk and chemical
67 properties. Sensor size, spatial position and orientation should be precisely controllable through in
68 situ microfabrication at cell and tissue-level length scales during live imaging. These structural
69 properties must be flexible and adaptable to detect inter-embryonic variability, providing a
70 generalizable solution which does not require prior knowledge of individual embryo morphology
71 or tissue mechanical properties.

72 Here, we describe development of a force quantification method applicable to vertebrate
73 morphogenesis by creating spring-like nano-Newton force sensors within living chicken embryos
74 by means of an intravital three-dimensional (i3D) bioprinting approach. i3D bioprinting has

75 previously been used to print millimetre-scale structures under mouse skin in vivo (16). We re-
76 developed this technique to enable micron-scale photo-crosslinking of biocompatible photo-active
77 polymers in a 3D elastic hydrogel. Combined with live-imaging microscopy, i3D-bioprinted
78 spring-like force sensors allow real-time quantification of neurulation mechanics. As proof of
79 principle, we demonstrate quantifiable disruption of closure mechanics in ROCK-inhibited
80 embryos.

81

82 **Results and Discussion**

83 **Bioprinting structures with defined geometry and material properties in embryos**

84 Two-photon i3D bioprinting enables creation of 3D shapes with high positional and structural
85 accuracy directly in confocal-imaged chick embryos (Figure 1A). Optimised experimental
86 conditions reproducibly produce pre-designed hydrogel structures in anatomically defined regions
87 of interest, namely the closing neural tube (Figure 1B). Hydrogel were made by two-photon
88 crosslinking 7-hydroxycoumarin-3-carboxylic acid functionalized polyethylene glycol backbones
89 (HCC-PEG) (16). The PEG polymeric backbone ensures full biocompatibility while its cell-
90 repellent properties minimize the undesired alteration of hydrogel tissue interface. The
91 photosensitive coumarin group allow high efficiency and versatility of polymeric crosslinking. A
92 star shape is shown to illustrate the range of printing dimensions over two orders of magnitude,
93 from ~1 μm at the tip ends to nearly 200 μm inter-tip span in the example shown (Figure 1B).
94 Alternative geometries can readily be defined and adapted to the closing neural tubes of individual
95 embryos (Figure 1C-D).

96 Closure of the neural tube requires medial apposition of the neural folds, physically narrowing the
97 open region and allowing progression of dorsal midline fusion by the “zippering point” (5, 17)
98 (schematically illustrated in Figure 1C). Neural tube zippering speed is not significantly affected
99 by i3D printing (Supplementary Figure 1A-B). As zippering advances and embryos continue to
100 develop, rigid i3D-printed structures can be displaced and ejected from the closing tube (Figure
101 1D, Supp Figure 1A). Their displacement indicates generation of mechanical forces by the embryo.
102 To quantify these forces, we adapted i3D bioprinting to create elastic, compliant shapes anchored
103 to the closing neural folds, such that their deformation serves as a readout of forces generated by
104 medial apposition of the neural folds (Figure 1C). We will refer to these structures as **intravital**
105 **mechano-sensory hydrogels (iMeSH)**.

106 A critical pre-requisite for this application is the ability to fine-tune iMeSH material properties.
107 We designed the polymeric backbone to act as an entropic spring. We found that 8-arm PEG 100%
108 functionalized with hydroxycoumarin-3-carboxylic acid allows tuneable control of hydrogel
109 stiffness (Young’s modulus) by adjusting laser powers. This will control the cross-linking degree
110 of coumarin groups (16) and will tune the PEG’s elastic response against conformational
111 deformations (Supplementary Figure 2A-B). We use the PEG concentration as an additional
112 parameter to control hydrogel compliance. Atomic force microscopy (AFM) of iMeSH structures
113 printed in the chick neural tube confirmed that Young’s modulus can be reproducibly adapted to
114 suit experimental needs (Figure 1F-G and Supplementary Figure 2C).

115 **Inferring morphogenetic mechanics from iMeSH deformation**

116 iMeSH structures stop closure of the adjacent neural tube, forming a localised open defect (Figure
117 2A, Supplementary Figure 3A). Over long timescales, fusion of the flanking zippering points
118 progresses to encircle the printed object (Supplementary Fig 3A-C), empirically dissociating local
119 mediolateral apposition from rostro-caudal zippering during RNP closure. iMeSH structures
120 printed freely within the neural tube are exteriorised during closure (Supplementary Fig 3D),
121 whereas structures anchored to the neuroepithelium become mediolaterally compressed within the
122 lumen (Figure 2B). Anchoring is achieved by partly overlapping the iMeSH photo-printing region
123 with the apical neuroepithelium, creating a hydrogel-tissue adhesive contact. We assayed various
124 potential iMeSH geometries, including complex shapes which undergo non-uniform deformations
125 when compressed (Supplementary Figure 4A-B), but ultimately selected a simple and adaptable
126 cylinder shape spanning the neural folds (Figure 2C).

127 Using a finite element method (FEM) based modelling, we derived a parameterised equation
128 whereby iMeSH cylinder deformation serves as a generalisable readout of force applied (Figure
129 2E-F and Supplementary Figure 5). Modelled cylinder narrowing, and contralateral elastic
130 expansion, is linearly related to the mechanical force applied by lateral contacts in a limited range
131 of deformation (Figure 2 F). Medial compression and perpendicular elongation of iMeSH cylinders
132 predicted *in silico* is observed *in vivo* (Figure 2G). At late developmental timepoints, after the
133 normal period of RNP closure, the neural tube continues to compress the iMeSH force sensor.
134 Cylinder mediolateral narrowing relative to its original width allows calculation of force (Figure
135 2H), although values obtained at these late timepoints should not be considered definitive given
136 the evolution of contact points around the cylinder's circumference. Force applied to the cylinder
137 is stored as elastic strain potential energy in the low pJ levels (Figure 2I). Converting this
138 mechanical energy value into a biological currency, 1 pJ can be stored in approximately 1×10^7
139 ATP molecules (18), although the biological conversion of chemical to mechanical energy is likely
140 to be highly inefficient.

141 We hypothesise that this energy derives from persistent actomyosin-dependent contractility of
142 cells surrounding the cylinder. Neuroepithelial F-actin retains its expected enrichment relative to
143 surrounding tissues in embryos with iMeSH cylinders between their neural folds (Figure 2J and
144 Supplementary Figure 3A).

145

146 **Neurulation requires pro-closure forces to exceed anti-closure forces**

147 The combination of iMeSH force-sensor bioprinting with time-lapse imaging makes it possible to
148 dynamically profile morphogenetic forces *in vivo* (Figure 3A-B). Medial apposition of the neural
149 folds applies an incremental compressive force to the iMeSH rim, causing it to displace medially
150 (Figure 3A). Forces compressing the iMeSH cylinder reach approximately 100 nN within a
151 developmentally-relevant window of one to two hours, before tending to decrease (Figure 1B).
152 Substantial pro-closure forces are known to be produced by planar-polarised apical constriction of
153 the neuroepithelium which elevates the neural folds (19, 20). We confirmed that the apical

154 neuroepithelium curves dorsally, but iMeSH structures suspended between the neural folds locally
155 resist this deformation (Supplementary Figure 6).

156 Pharmacologically inhibiting the myosin-activating kinase ROCK is known to stop neural fold
157 elevation in chick and mammalian embryos (19, 20). We observed progressive widening of the
158 neural folds in ROCK-inhibited embryos (Figure 3C). This presents an additional force
159 quantification challenge: force sensors simply placed between the neural folds only deform when
160 the surrounding tissue compresses them. Anchoring iMeSH cylinders directly to embryonic tissue
161 solves this problem, allowing them to be stretched by tissue expansion (Figure C-E). Ignoring the
162 direction of force application, the maximum elastic strain energy imparted into the iMeSH cylinder
163 during live-imaging is significantly lower in ROCK-inhibited than control embryos (Figure 3F).
164 ROCK-inhibited embryos also generate less force per unit time than vehicle controls: their
165 maximum impulse within 60 minutes is significantly lower (Supplementary Figure 7).
166 Nonetheless, it is remarkable that the absolute anti-closure energy imparted, and impulse
167 generated, by ROCK-inhibited embryos are comparable to the pro-closure equivalents in controls.

168 Thus, iMeSH force sensors printed with high spatial resolution and positional accuracy, combined
169 with time-lapse live imaging, permit quantification of the mechanical energy generated during
170 vertebrate neural tube closure. This technology is highly versatile, readily accommodating
171 differences in initial embryo morphology and direction of force generation, allowing dynamic
172 profiling of both compressive and stretching forces. Application of this technology has already
173 provided unexpected insights into the delicate balance between pro- and anti-morphogenetic forces
174 which, when disrupted, may produce severe birth defects.

175

176

177

178

179

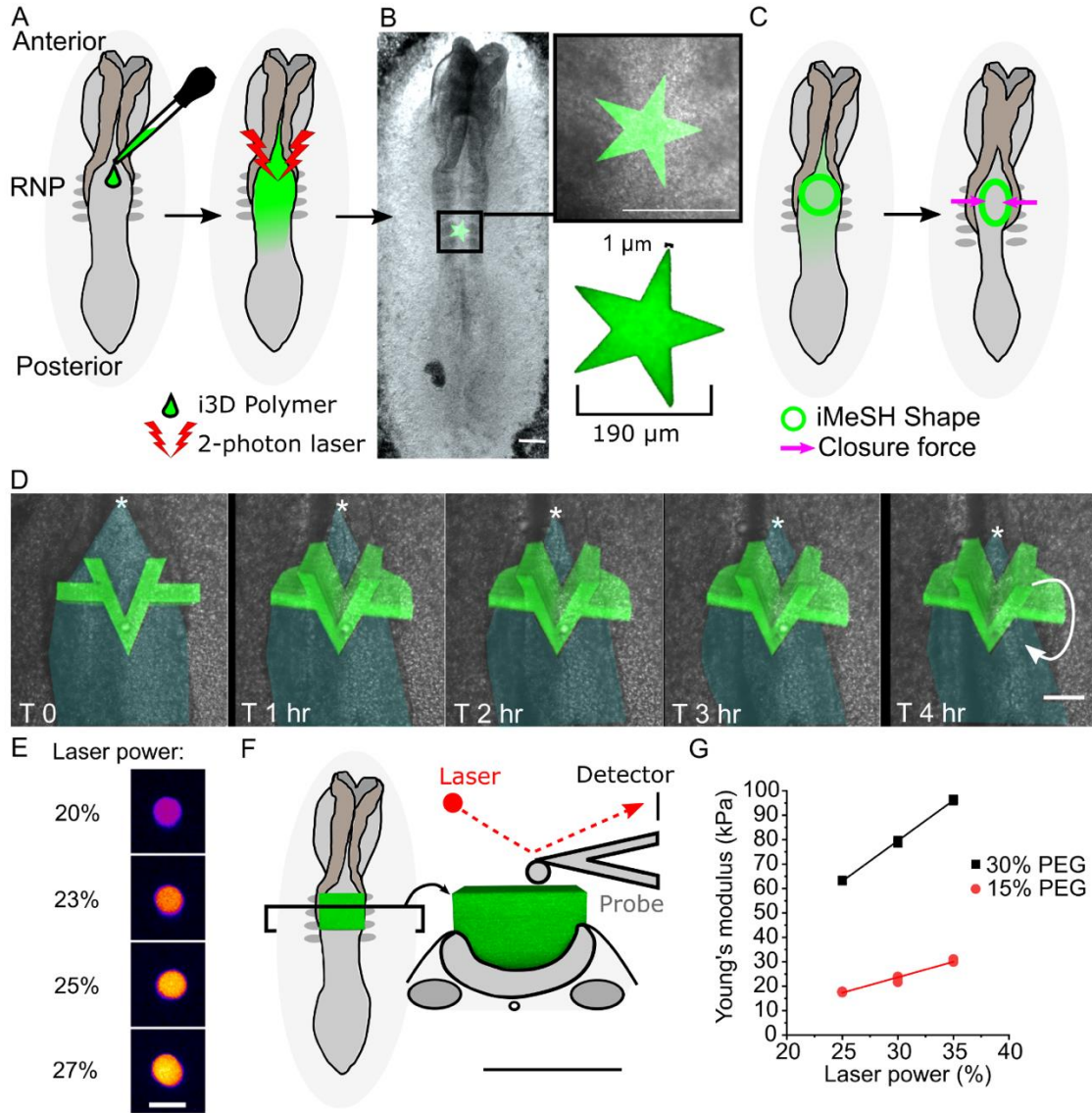


Figure 1: i3D bioprinting with accurately determined position, geometry, and stiffness. (A) Schematic of a chicken embryo illustrating the experimental workflow. 2-3 μl i3D polymer is pipetted directly onto the rhombocervical neuropore (RNP) and photo-polymerised with a 2-photon laser. iMeSH structures are shown in green throughout. (B) Stereoscope image of an embryo with a star shape photo-polymerised on the flat neural plate. Scale bar = 200 μm . The star dimensions are indicated. (C) Schematic showing iMeSH compression by apposition of the neural folds. (D) Time-lapse images showing sequential displacement of a rigid iMeSH shape shown as a 3D confocal reconstruction superimposed on the embryo imaged with transmitted light. Cyan shading = open neural tube, * = zippering point, arrow indicates rotation of the printed shape, scale bar = 50 μm . (E) Fire lookup table showing autofluorescence of iMeSH photo-polymerised with the indicated laser powers on the same embryo. Scale bar = 25 μm . (F) Schematic illustration of AFM stiffness testing of an iMeSH shape. 3D reconstructions of the shape are shown superimposed on a dorsal and transverse schematic of the embryo. Scale bar = 100 μm . (G) AFM quantification of iMeSH polymerised on the same embryo at the indicated laser powers. The values were calculated from AFM indentations performed at a rate of 0.5 $\mu\text{m}/\text{s}$ and depths of 1 μm (30% w/w HCC-PEG) or 2 μm (15% w/w HCC-PEG).

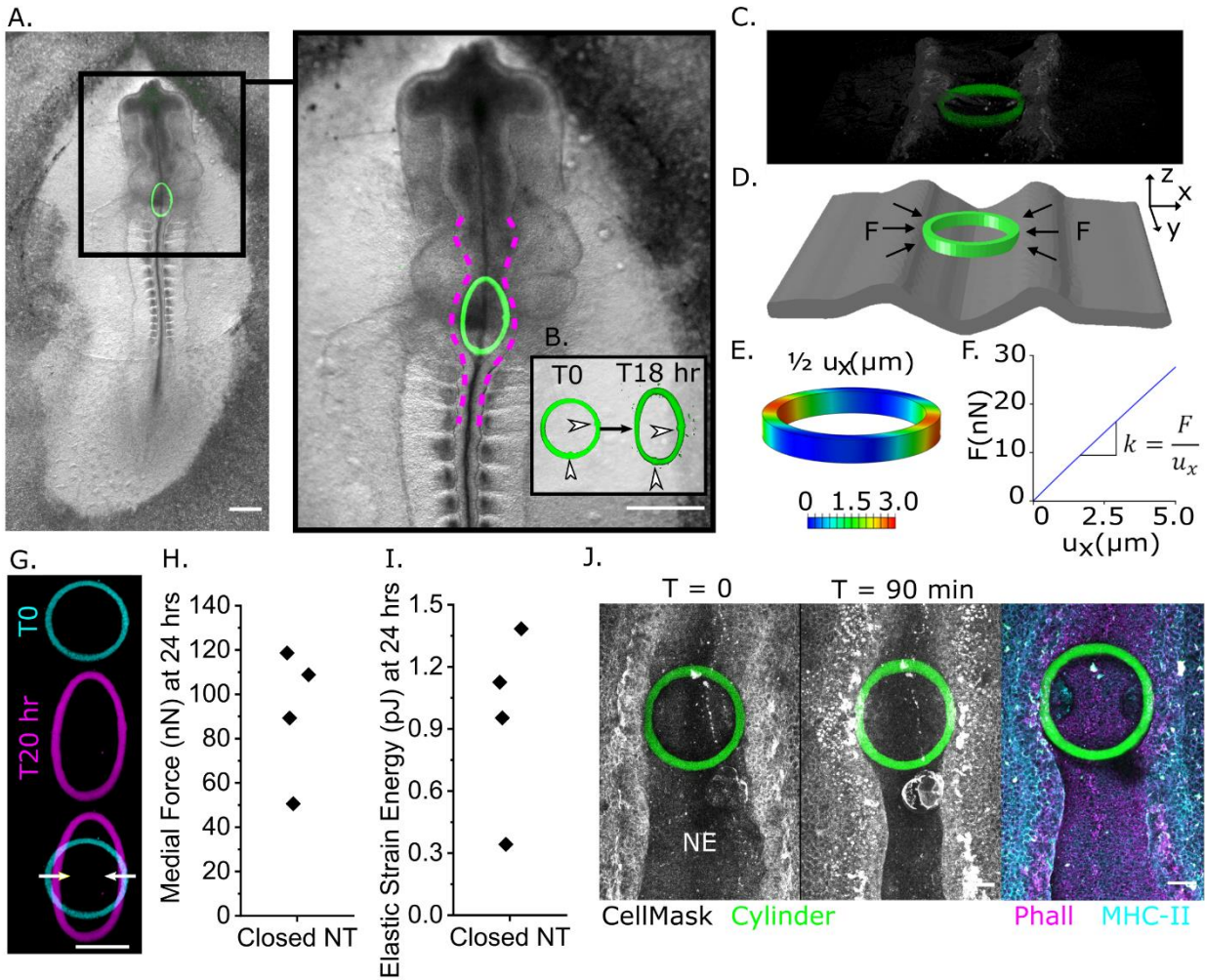


Figure 2: Quantification of medial force applied by the closed neural tube. (A) Brightfield view of a chick embryo 18 hours after an iMeSH cylinder (green) was bio-printed within its open neural tube. Dashed lines indicate the neural folds. Scale bar = 500 μm . (B) Confocal 3D reconstructions of the cylinder in the same embryo following bio-printing and 18 hours later. Arrowheads indicate small landmarks incorporated in the cylinder, demonstrating minimal rotation. (C) Oblique view of an iMeSH cylinder incorporated within the neural folds of a representative chick embryo. Scale bar = 100 μm . (D) Finite element model of an iMeSH cylinder and surrounding tissue based on 3D reconstruction of the specific morphometry, with representation of contact forces between tissue and cylinder. In the reference system, x is the medial-lateral direction, y the cranio-caudal direction and z the dorsoventral direction. (E) Contours of absolute displacement in the mediolateral direction (u_x). (F) Resultant contact force (F) versus narrowing in the mediolateral direction. The slope of the curve corresponds to the cylinder stiffness, k . (G) Projected image of a cylinder printed in a chicken RNP immediately after printing and in a deformed state within the lumen of the neural tube 20 hours later. Scale bar = 100 μm . (H-I) Quantification of (H) medial force applied and (I) elastic strain energy stored within compressed cylinders incorporated in partially closed neural tube 16-20 hours after printing. Points represent individual embryos. (J) Representative embryo immediately after iMeSH printing and 90 minutes later. The same embryo was fixed and stained for actomyosin. NE = neuroepithelium, scale bars = 50 μm .

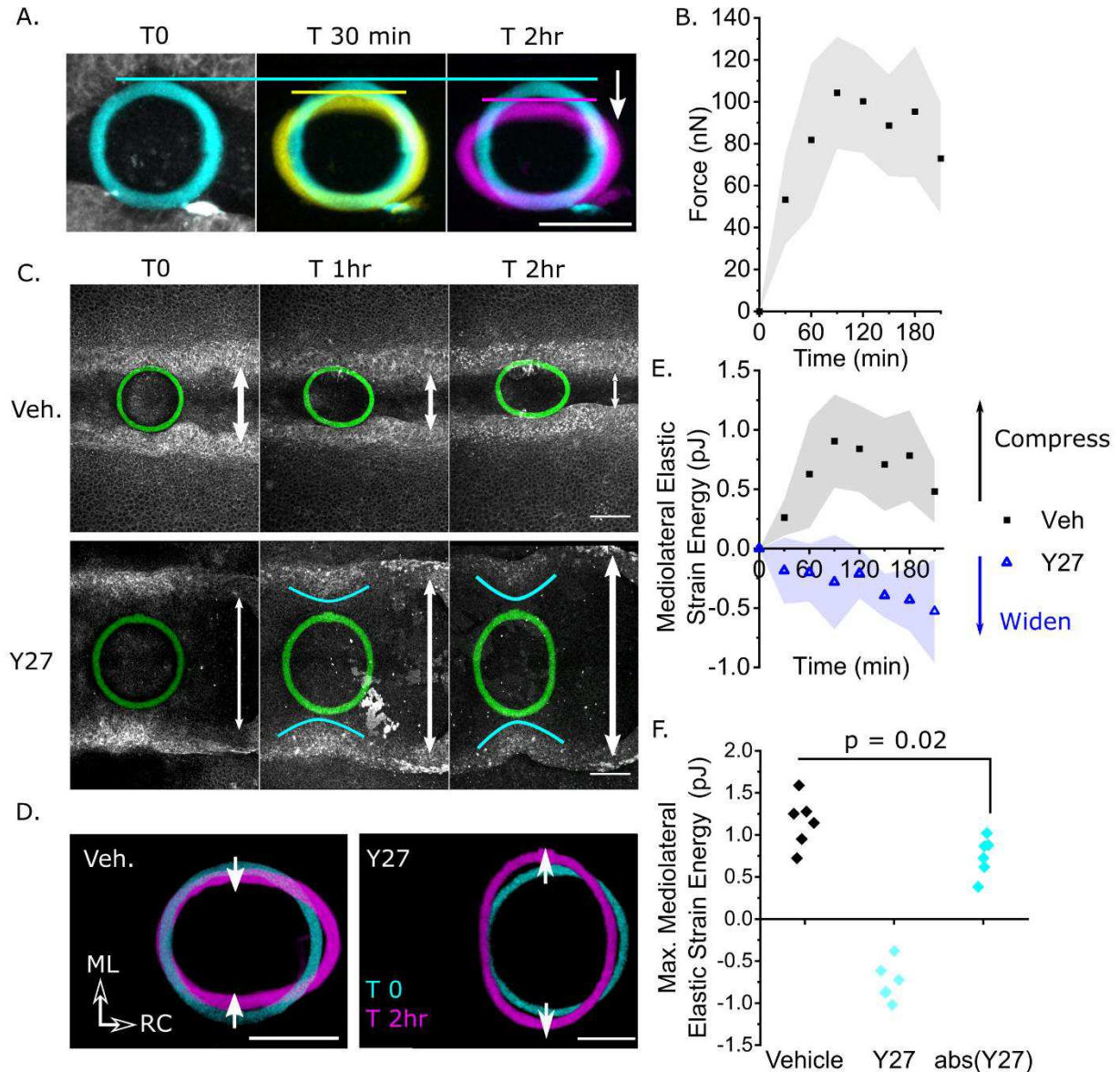


Figure 3: Dynamic quantification of morphogenetic mechanics during neurulation. (A) Illustrative iMeSH cylinder showing progressive medial displacement (arrow). Scale bar 50 μ m. (B) Dynamic profiling of medial compressive force. Points represent the mean \pm 95% CI, n = 6 vehicle-treated embryos. (C) Sequential images at indicated timepoints in a vehicle-treated embryo and one treated with 20 μ M of the ROCK inhibitor Y27632 (Y27). White arrows indicate the width of the neuropore. Cyan lines illustrate bending of the neural folds as they pull on the attached iMeSH cylinder. Scale bar 100 μ m. (D). 3D reconstructions of the iMeSH cylinders in A. ML mediolateral, RC rostrocaudal. Scale bars 100 μ m. (E) Average mediolateral potential energy stored in the iMeSH cylinder over time. Points represent the mean \pm 95% CI, n = 6 per group. (F) Dynamic profiling of mediolateral elastic strain energy in the iMeSH cylinder. Points represent the mean \pm 95% CI, n = 6 per group, vehicle embryos are those force-profiled in B. (G) Maximum potential energy imparted by each embryo during live imaging. Points represent independent embryos. Vehicle embryos are compared against the absolute (non-directional) values of Y27-treated embryos by T-test.

References

1. M. Zhu, M. Zernicka-Goetz, Principles of Self-Organization of the Mammalian Embryo. *Cell* **183**, 1467-1478 (2020).
2. C. Collinet, T. Lecuit, Programmed and self-organized flow of information during morphogenesis. *Nat Rev Mol Cell Biol* **22**, 245-265 (2021).
3. B. Boyle *et al.*, Estimating Global Burden of Disease due to congenital anomaly: an analysis of European data. *Arch Dis Child Fetal Neonatal Ed* **103**, F22-F28 (2018).
4. I. Zaganjor *et al.*, Describing the Prevalence of Neural Tube Defects Worldwide: A Systematic Literature Review. *PLoS one* **11**, e0151586 (2016).
5. E. Nikolopoulou, G. L. Galea, A. Rolo, N. D. Greene, A. J. Copp, Neural tube closure: cellular, molecular and biomechanical mechanisms. *Development* **144**, 552-566 (2017).
6. L. A. Davidson, R. E. Keller, Neural tube closure in *Xenopus laevis* involves medial migration, directed protrusive activity, cell intercalation and convergent extension. *Development* **126**, 4547-4556 (1999).
7. S. Y. Sokol, Mechanotransduction During Vertebrate Neurulation. *Curr Top Dev Biol* **117**, 359-376 (2016).
8. G. L. Galea *et al.*, Biomechanical coupling facilitates spinal neural tube closure in mouse embryos. *Proceedings of the National Academy of Sciences of the United States of America* **114**, E5177-E5186 (2017).
9. E. Maniou *et al.*, Hindbrain neuropore tissue geometry determines asymmetric cell-mediated closure dynamics in mouse embryos. *Proceedings of the National Academy of Sciences of the United States of America* **118**, (2021).
10. G. L. Galea *et al.*, Cell non-autonomy amplifies disruption of neurulation by mosaic *Vangl2* deletion in mice. *Nat Commun* **12**, 1159 (2021).
11. E. Nikolopoulou *et al.*, Spinal neural tube closure depends on regulation of surface ectoderm identity and biomechanics by *Grhl2*. *Nat Commun* **10**, 2487 (2019).
12. L. A. Davidson, Embryo mechanics: balancing force production with elastic resistance during morphogenesis. *Curr Top Dev Biol* **95**, 215-241 (2011).
13. N. I. Petridou, C. P. Heisenberg, Tissue rheology in embryonic organization. *EMBO J* **38**, e102497 (2019).
14. A. Mongera *et al.*, A fluid-to-solid jamming transition underlies vertebrate body axis elongation. *Nature* **561**, 401-405 (2018).
15. L. A. Afman, H. J. Blom, N. M. Van der Put, H. W. Van Straaten, Homocysteine interference in neurulation: a chick embryo model. *Birth Defects Res A Clin Mol Teratol* **67**, 421-428 (2003).
16. A. Urciuolo *et al.*, Intravital three-dimensional bioprinting. *Nat Biomed Eng* **4**, 901-915 (2020).
17. L. D. Moon, F. Xiong, Mechanics of neural tube morphogenesis. *Semin Cell Dev Biol*, (2021).
18. F. Meurer, H. T. Do, G. Sadowski, C. Held, Standard Gibbs energy of metabolic reactions: II. Glucose-6-phosphatase reaction and ATP hydrolysis. *Biophys Chem* **223**, 30-38 (2017).
19. M. B. Butler *et al.*, Rho kinase-dependent apical constriction counteracts M-phase apical expansion to enable mouse neural tube closure. *J Cell Sci* **132**, (2019).
20. T. Nishimura, H. Honda, M. Takeichi, Planar cell polarity links axes of spatial dynamics in neural-tube closure. *Cell* **149**, 1084-1097 (2012).

Acknowledgements

The authors wish to thank Mr Ioakeim Ampartzidis, Dr Federica Michielin, and Professors Andrew Copp, Nicholas Greene and Paolo de Coppi for their critical discussion of this project. GLG is supported by the Wellcome Trust (211112/Z/18/A and 11112/Z/18/Z). NE is supported by University of Padova, Progetti di Eccellenza Cariparo, TWINING of University of Padova, Oak Foundation Award. Core facilities in the UCL GOS Institute of Child Health are supported by the NIHR GOSH Biomedical research centre. The CMII 23S antibody developed by Conrad, G.W./Conrad, A.H., Kansas State University, was obtained from the Developmental Studies Hybridoma Bank, created by the NICHD of the NIH and maintained at The University of Iowa, Department of Biology, Iowa City, IA 52242. The authors wish to thank Onyel Biotech s.r.l. (Italy) for helping in the synthesis of photosensitive polymers.

Author contributions

GLG, NE designed the study and wrote the manuscript. EM performed the main experiments and analysed the data, with help from GLG. ST and PP developed the FEM and analysed data. DM, AU and MM helped with the experimental setup of 3D bioprinting. AU and MG performed AFM analysis. GLG, NE, EM, AU, ST critically discussed the data and manuscript. GLG and NE supervised the project and provided funding. All authors approved the manuscript.

Quantifying mechanical forces during vertebrate morphogenesis

Eirini Maniou¹, Silvia Todros², Anna Urciuolo^{2,3}, Dale Moulding¹, Michael Magnusson¹, Monica Giomo², Piero G. Pavan^{2,3}, Gabriel L Galea^{1,*}, Nicola Elvassore^{1,2,*}

* These authors contributed equally. Order determined by coin toss.

1. Developmental Biology and Cancer, UCL GOS Institute of Child Health
2. Department of Industrial Engineering, University of Padova, via Venezia 1, 35131 Padova, Italy
3. Fondazione Istituto di Ricerca Pediatrica Città della Speranza, Corso Stati Uniti 4, 35127 Padova, Italy

Table of contents

Materials and methods:.....	2
Chick embryo culture and inhibitor treatment.....	2
Bioprinting and time-lapse live imaging	2
Immunostaining	2
Image analysis and force quantification.	3
AFM-based force spectroscopy	3
In silico analysis of neural tube/cylinder interaction.....	3
Estimation of i3D cylinder nominal stiffness	4
Statistical analysis	4
Supplementary figures and legends	6
Supplementary Figure 1: i3D printing does not diminish neural tube zippering.....	6
Supplementary Figure 2: Reproducibility of Young’s modulus of i3D bioprinted structures.	7
Supplementary Figure 3: i3D cylinder incorporation within the closing neural tube.....	8
Supplementary Figure.....	10
Supplementary Figure 5: Development of Finite Elements Models (FEM) and derivation of a parametrized equation to evaluate force.	12
Supplementary Figure 6: i3D cylinder locally resist neuroepithelial bending.	14
Supplementary Figure 7: Maximum impulse generated during chick neural fold apposition.	15
Supplementary References.....	16

Materials and methods:

Chick embryo culture and inhibitor treatment

Fertile Dekalb white eggs (Henry Stewart, Norfolk, UK) were incubated at 37°C for 34 hours to reach Hamburger and Hamilton stage 8. Embryos were dissected and put in EC culture following a published protocol (1). Excess yolk was washed off using Pannett-Compton saline. Embryos with rhombocervical or posterior neuropores were selected. The vitelline membrane was windowed using a tungsten needle to expose the neuropore. For inhibitor studies, ROCK inhibitor (Y27632; Cell guidance systems, Cambridge) was reconstituted with PBS at stock concentration of 10 mM. The inhibitor was mixed with agar-albumen for preparation of EC culture plates at final concentration of 10 μ M (n = 3) or 20 μ M (n = 3): no differences were observed between these concentrations so they were combined for all analyses. For live imaging, the embryos were transferred to the inhibitor plates just prior to vitelline membrane windowing and were exposed to the inhibitor for 20 min before the start of imaging.

Bioprinting and time-lapse live imaging

After vitelline membrane windowing, embryos were stained with 1:100 CellMaskTM Deep Red plasma membrane (C10046 Invitrogen, Paisley) in PBS for 15 min at 37 deg. Excess CellMaskTM was washed off with PBS. For inhibitor studies, Y27632 was diluted at 20 μ M with CellMaskTM and PBS for staining and washing respectively. 3 μ l of 30% HCC-8-arm PEG in DPBS were added on the embryo over the neuropore. The embryo was then moved to the heated stage (37 deg) of a Zeiss Examiner LSM 880 confocal for bioprinting. Cylinders were drawn as ROIs in ZEN 2.3 software overlapping with the neural folds for attachment. Two-photon hydrogel cross-linking was performed using a 20X/NA 0.7 EpiPlan Apochromat dry objective (WD 1.3 mm). Printing was performed using a Mai Tai laser (SpectraPhysics Mai Tai eHP DeepSee multiphoton laser) at 700 nm and 30% laser power. X/Y pixels were 0.25 μ m, standard pixel dwell time 0.47 μ s, z step: 0.7 μ m and averaging 4. Live imaging was performed using the same objective with X/Y pixel 0.59 μ m and z step of 1 μ m (pixel dwell time 0.77 μ s, speed 8, averaging 1, bidirectional imaging, 1024 x 1024 pixels). Imaging lasers used were 488 nm at 1% and 633 nm at 0.50% laser power in order to obtain morphologically accurate information with minimal phototoxicity. The time step was 30 min.

Immunostaining

Images are representative of observations in at least three independent embryos. The primary antibody against Myosin IIb (CMII 23s) was purchased from Developmental Studies Hybridoma Bank at stock concentration of 44 μ g/mL. Embryos were fixed with 4% PFA overnight at 4 deg. They were permeabilised with 0.1% Triton X-100 in PBS (PBT) for 1 h at room temperature, blocked overnight in 5% BSA/PBT at 4 °C and incubated in 1:10 dilution of primary antibody in blocking solution. After 3x 30 min washes in blocking solution at room temperature, the embryos were incubated in a 1:500 dilution of Alexa Fluor 568-conjugated secondary antibody

(Life Technologies) and 1:200 Phalloidin 647 (Invitrogen), both in blocking solution. Excess secondary antibody was removed by washing with PBT at room temperature. For imaging, stained embryos were held in place with tungsten needles on 4% agar dishes and imaged in PBS on Zeiss LSM880 confocal. The objective was dipping 10X/NA 0.5 Plan Apochromat with X/Y pixel sizes of 0.83 μm and z step of 2.78 μm (pixel dwell time 0.77 μs , speed 8, averaging 2, bidirectional imaging, 1024 x 1024 pixels). Images were processed with ZEN 2.3 software and visualized as maximum or 3D projections in Fiji (2).

Image analysis and force quantification.

Acquired sequences were registered using Fiji plugins correct 3D drift and StackReg. Cylinder deformation was measured in Fiji using bounding rectangle. Following registration, zippering rate was calculated using Fiji manual tracking plugin and chemotaxis tool (Ibidi). Cylinder dimensions were measured in a confocal image acquired immediately after i3D printing using line tools in Fiji. In order to calculate the cylinder's width, maximum projections of all time points were registered using rigid body registration with StackReg in Fiji, the cylinder was manually outlined and its mediolateral width measured using the bounding rectangle tool. Force was calculated from mediolateral deformation of the cylinder using a parametrized equation (see Supplementary Figure 5). Work, which results in potential energy stored within the force sensor, was calculated as the area under the force versus displacement curve. Impulse was calculated as force generated within each 60-minute period, multiplied by time.

AFM-based force spectroscopy

Measurements were conducted using a XE Bio AFM (Park Systems, South Korea). The force-displacement curves were acquired using PPP-CONTSCR-10 pyramidal tips mounted on Si₃N₄ cantilevers with a nominal spring constant of 0.2 N/m (NanoSensors, Neuchatel, Switzerland). Cantilever spring constants were calibrated by the manufacturer prior use. The sensitivity of each cantilever was adjusted by measuring the slope of force-distance curve acquired on a hard reference material prior to each experiment. Indentation experiments were repeated at least three times for each sample, at different locations. All AFM measurements were done in a fluid environment (PBS) at room temperature. The Young's modulus was calculated applying a fit of the Hertz model to the force-distance curve, assuming a Poisson ratio of 0.5.

In silico analysis of neural tube/cylinder interaction

Finite Element Method (FEM) based numerical models were developed by means of ABAQUS CAE/ABAQUS Standard (SIMULIA™, Dassault Systems®). FEM models of iMeSH cylinders and neural tube tissue were obtained from the 3D geometry of representative experiments. The mechanical behaviour of hydrogel and the passive behaviour of tissue were described with an isotropic hyperelastic almost-incompressible neo-Hookean model, included in ABAQUS

material library. The constitutive parameters were set to correspond with a Young's modulus $E = 80$ kPa and 25 kPa, for the hydrogel and the tissue respectively. The values of Young's modulus were measured through AFM indentation. Cylinder and tissue solid regions were meshed with hexahedral and tetrahedral elements respectively, both with hybrid formulation to avoid numerical instabilities due to the almost-incompressible behaviour. Nonlinear static analysis was carried out simulating the progressive shifting of tissue folds and the corresponding deformation of the cylinder, up to the displacement values measured experimentally on the cylinder diameter in the medial-lateral direction. Contact forces between tissue and cylinder surfaces were computed from numerical results as index of the closing capability of tissue. FEM models allow to precisely estimate the contact forces for very general conditions of cylinder and tissue interaction, also including the evolution of contact surface around the cylinder's circumference at large deformations of the iMeSH.

Estimation of i3D cylinder nominal stiffness

In the case of small deformation and limited contact surface between tissue and iMeSH, FEM models with a simplified geometry can be developed to evaluate the structural stiffness of the i3D cylinder when varying different parameters. In detail, several models were considered, varying cylinder height H between $20 \mu\text{m}$ and $100 \mu\text{m}$, diameter D between $140 \mu\text{m}$ and $220 \mu\text{m}$, wall thickness T between $5 \mu\text{m}$ and $25 \mu\text{m}$, and hydrogel Young's modulus E between 5 kPa to 80 kPa. Neural tissue folds were modelled as two rigid surfaces which were progressively getting closer in the medial-lateral direction. The contact force between cylinder and rigid surfaces was computed from numerical analyses of each different condition and the corresponding cylinder stiffness k was obtained as a ratio between contact force and medial-lateral displacement. In the case of small deformation, the stiffness k can be approximated as a constant k' obtained through a parametric equation of the type:

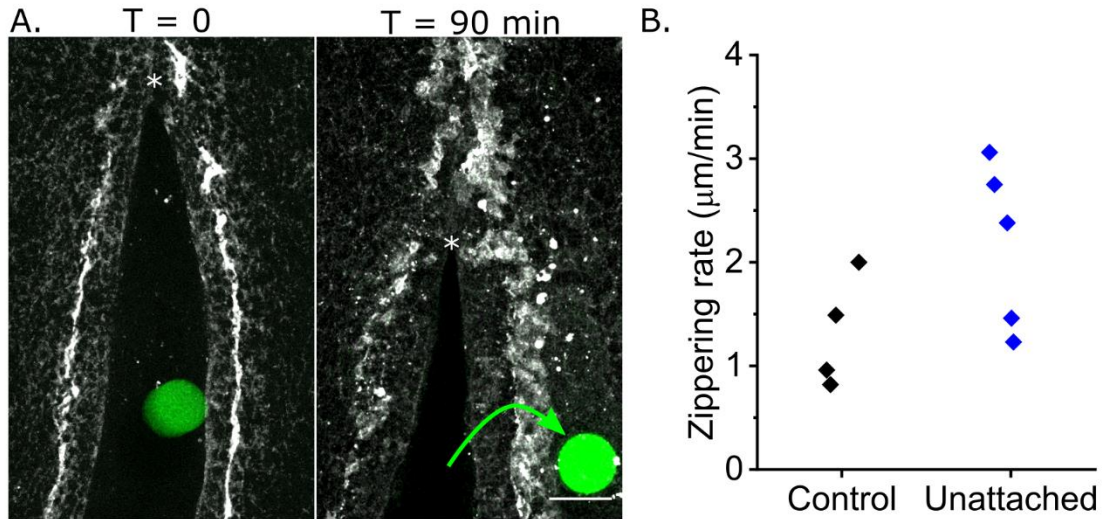
$$k' = \alpha \cdot H \cdot \left(\frac{T}{D}\right)^3 \cdot E$$

where α is fitting constant to be determined from the overall set of numerical results by means of an optimization procedure based on the least-squares method. The optimization procedure was implemented in a user-routine developed in the open-source software Scilab (version 6.1.0, Esi Group, Paris, France), obtaining $\alpha = 7.718 \mu\text{m}^{-1}$. This parametric equation allows evaluation of nominal stiffness of the cylinder depending on its size (height, diameter and thickness) and Young's modulus, in the above-mentioned ranges for the different parameters. Once the displacement of the cylinder diameter in the medial-lateral direction is measured from an experiment, it is used as an input, and the contact force between tissue and cylinder can be estimated at each time instant by multiplying by the stiffness k' .

Statistical analysis

For qualitative endpoints, observations were made in at least three independent embryos. For quantitative endpoints, individual embryos were the unit of measure. Statistical comparisons between two groups of normally-distributed data and equal homogeneity of variance were by two-tailed T-test in Origin 2020.

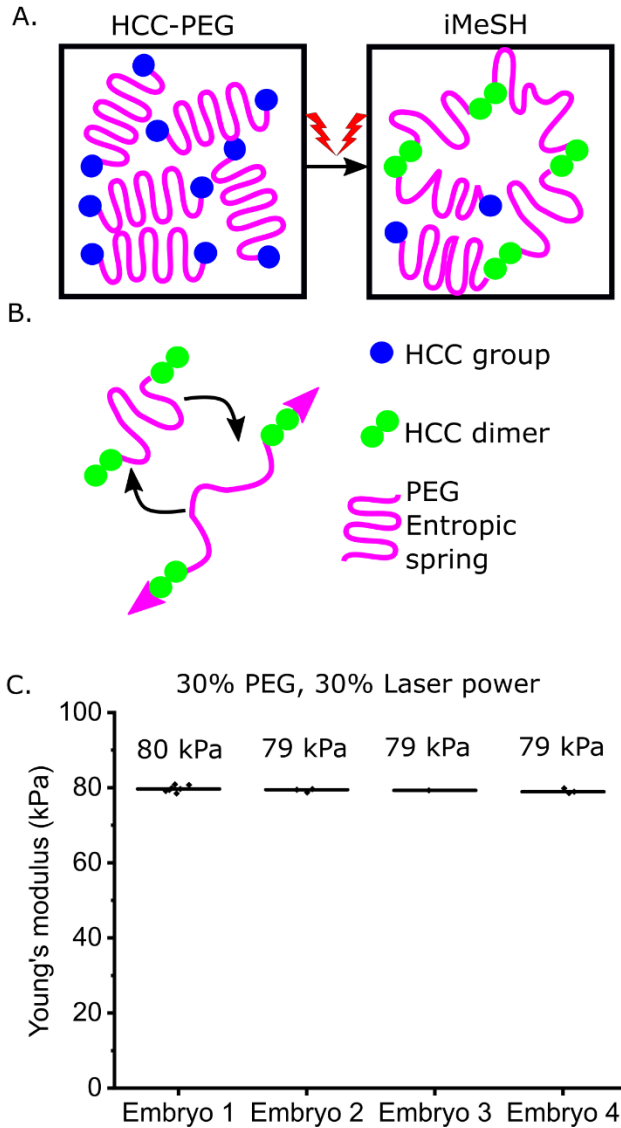
Supplementary figures and legends



Supplementary Figure 1: i3D printing does not diminish neural tube zippering.

A. Sequential confocal images of a chick embryo posterior neuropore soon after i3D printing a pillar between its neural folds but not attached to its tissues, and 90 minutes later when the unattached cylinder had been extruded from the neuropore (green arrow). * indicates the zippering point, scale bar = 50 μm .

B. Quantification of rate of zippering point progression in the posterior neuropores of control embryos live-imaged without i3D printing and in embryos with unattached pillars printed inside their neuropore lumen. Points represent individual embryos.

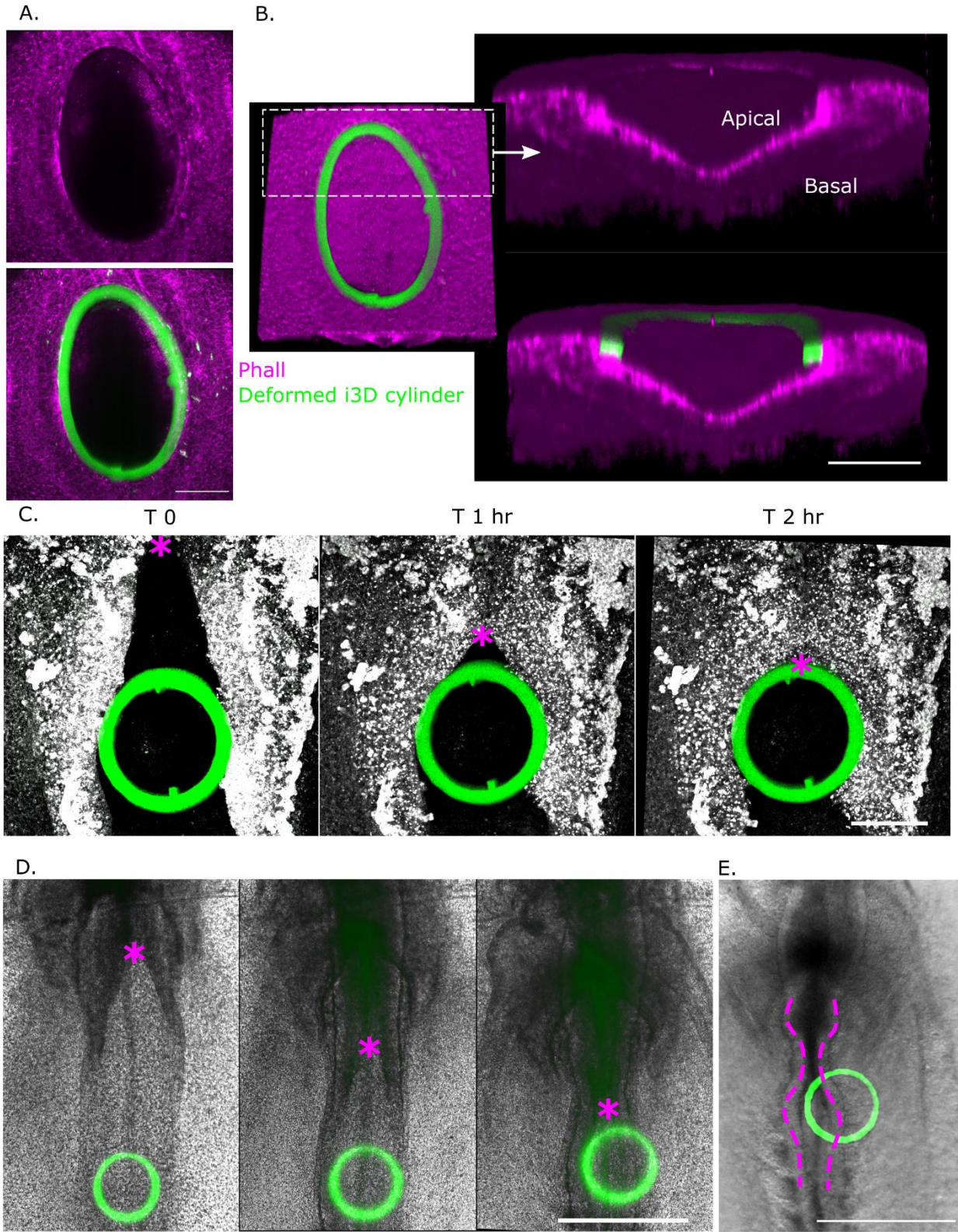


Supplementary Figure 2: Reproducibility of Young's modulus of i3D bioprinted structures.

A. Schematic showing conversion of HCC-PEG polymer into an iMeSH structure through photocrosslinking using two-photon irradiation.

B. Schematic illustration of elastic PEG deformation caused by force application (magenta arrows).

C. AFM quantification of Young's modulus of i3D shapes printed in four different embryos with equivalent polymerisation settings. The results have been derived from force-distance curves recorded at indentation depths of 3 μm and rates of 0.3 $\mu\text{m/s}$ (Embryo 1,2,4) or 0.5 $\mu\text{m/s}$ (Embryo 3).



Supplementary Figure 3: i3D cylinder incorporation within the closing neural tube.

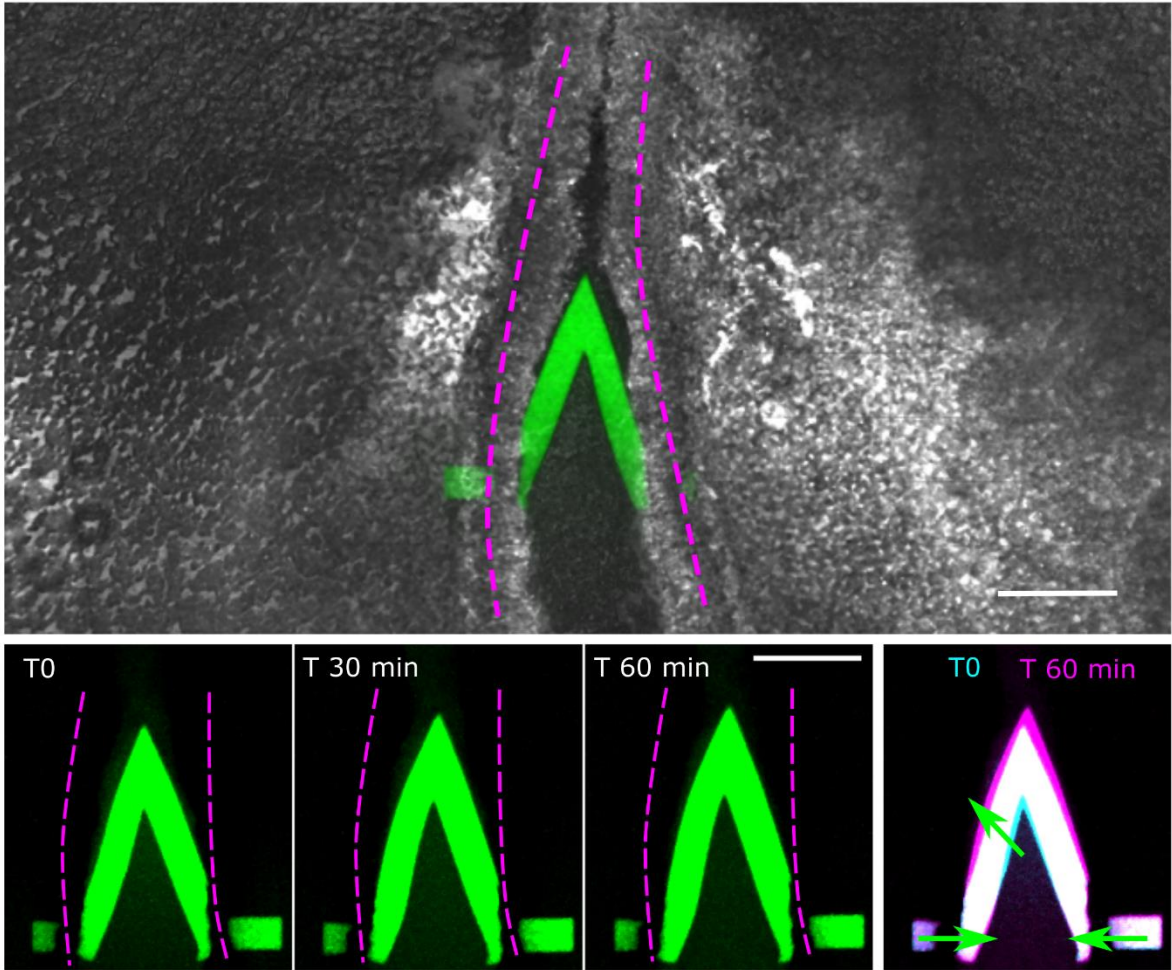
A-B. Representative embryo showing encircling of an i3D cylinder by the surface ectoderm and neural folds, leaving an open defect, shown as A) maximum projections and B) 3D confocal reconstructions. Note the persistent apical enrichment of phalloidin-labelled neuroepithelial F-actin. Scale bar = 100 μm .

C. Live-imaging of a CellMask-labelled embryos showing progression of rostral-to-caudal zippering (*) until it encircles a stiff cylinder incorporated within its neural folds. Scale bar = 100 μm .

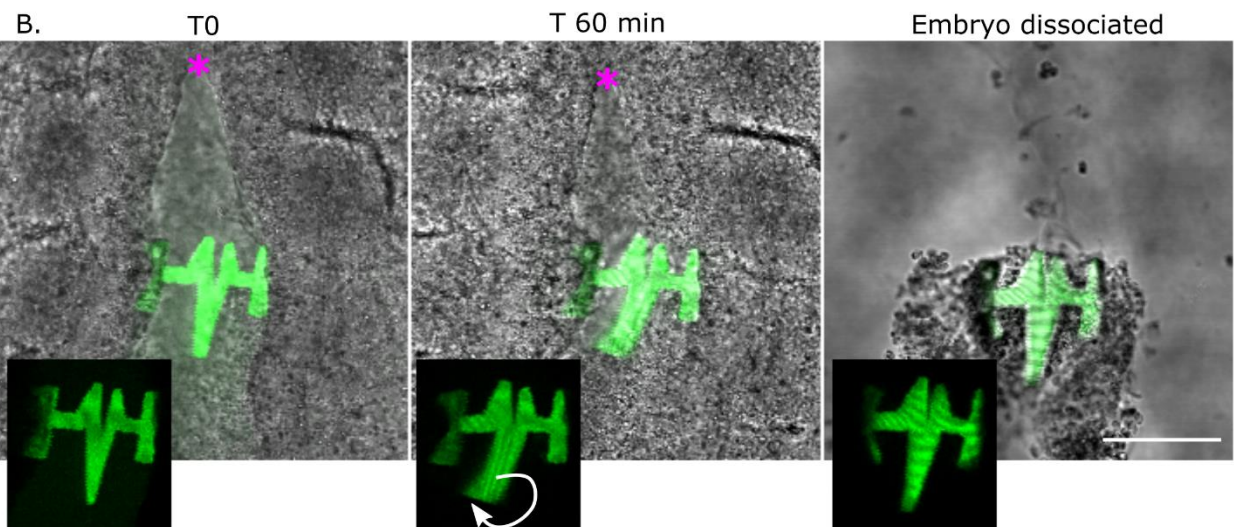
D. Partial extrusion of an i3D cylinder not entrapped within the closing neural folds of a chick embryo. Note progression of zippering (*) and lack of cylinder compress. Scale bar = 400 μm .

E. Brightfield image of the embryo in C 18 hours after cylinder polymerisation. Dashed magenta lines indicate the neural folds. Scale bar = 400 μm .

A.



B.

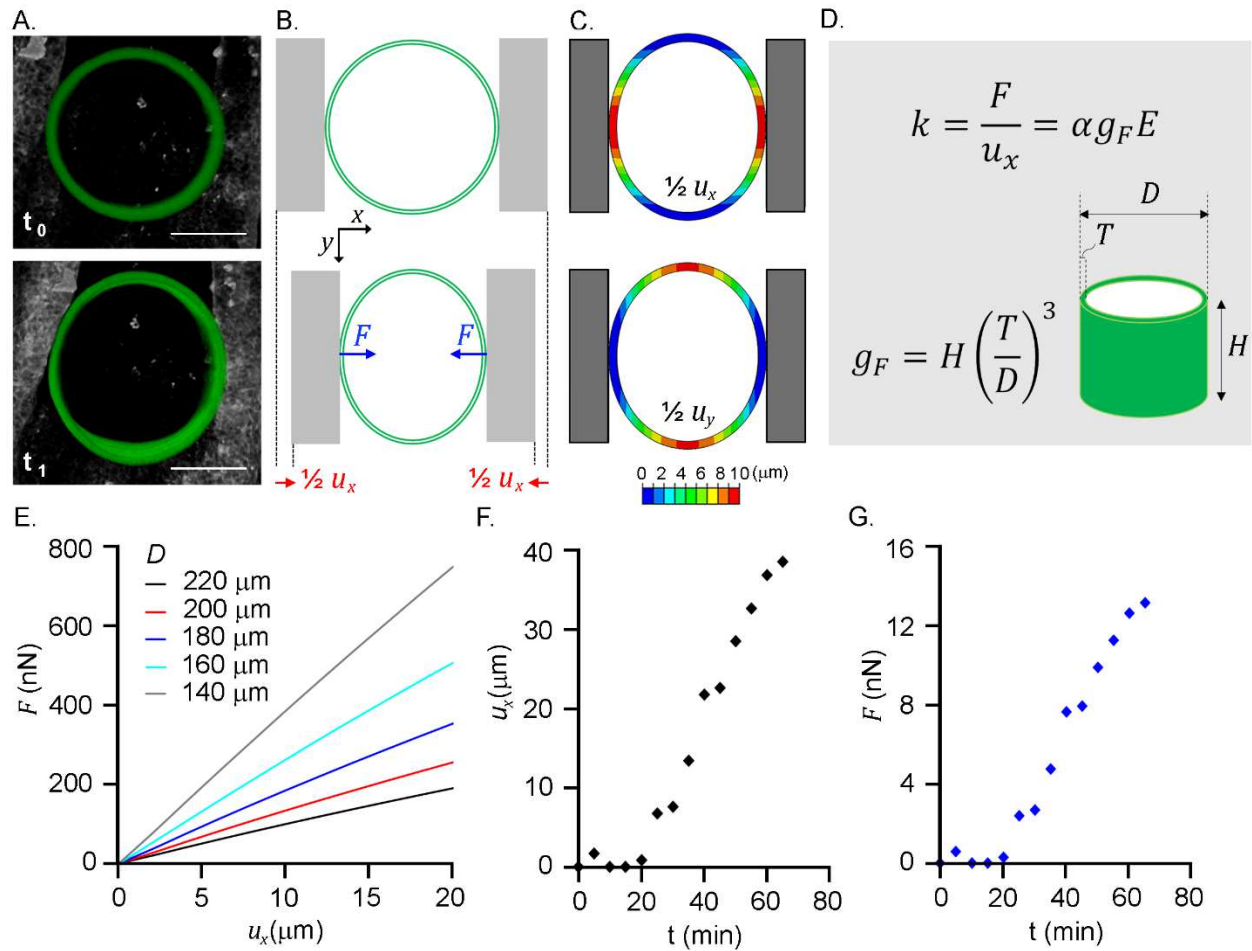


Supplementary Figure 4: Complex deformation of non-cylindrical i3D bioprinted shapes.
Note these examples show printing within the posterior neuropore, not the RNP used in the rest of this study.

A. Reflection imaging (grey) of a chicken embryo with an i3D bioprinted V-shaped spring (green), shown as 3D confocal reconstructions below. Magenta dashes lines indicate the neural folds, green arrows indicate the complex deformations of the spring between T0 and T 60 mins.

B. Brightfield and confocal 3D images of an alternative spring spanning the neural folds caudal to the zippering point (*). The curved white arrow indicates lateral rotation of the ventral spring tip, which is elastically reversed by largely dissociating the embryo through prolonged incubation.

Scale bars = 100 μm .



Supplementary Figure 5: Development of Finite Elements Models (FEM) and derivation of a parametrized equation to evaluate force.

A. Dorsoventral view of an i3D cylinder incorporated within the neural folds of a representative chick embryo at different time points ($t_0 = 0$, $t_1 = 65$ min). Scale bar = $100 \mu\text{m}$.

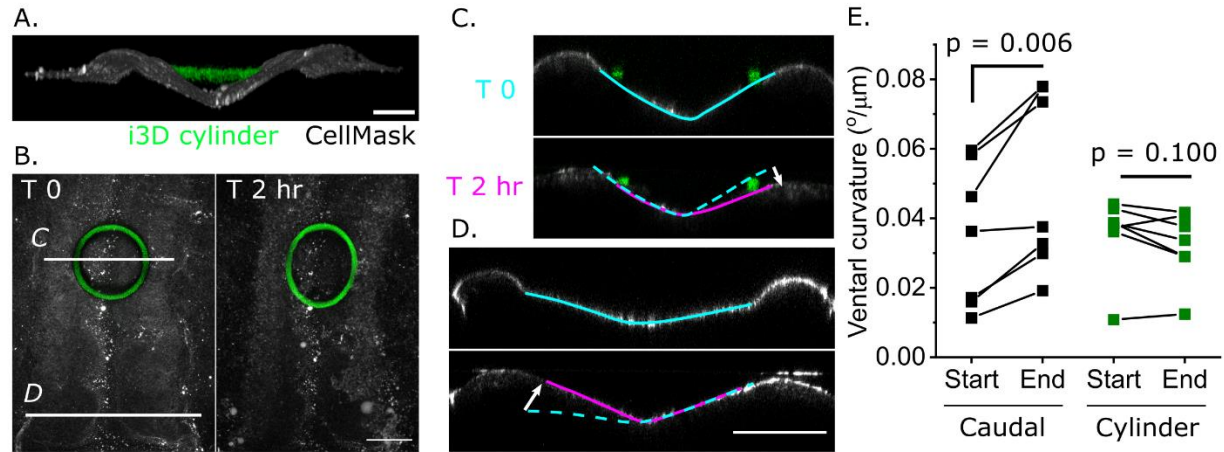
B. Scheme showing the compressive force F on the cylinder walls, due to the growth and folding of the neural tube, and the corresponding deformation of the cylinder. In the reference system, x is the medial-lateral direction and y the cranio-caudal direction.

C. Contours of absolute displacement in the medial-lateral direction (u_x) and in the cranio-caudal direction (u_y). The cylinder narrowing in the medial-lateral direction from experimental data is the input of numerical analysis, which allows to estimate the corresponding contact force.

D. The cylinder stiffness k , as the ratio between the contact force F and the displacement u_x , is proportional to the hydrogel Young's modulus E and to a geometric factor g_F , which depends on cylinder height H , diameter D and wall thickness t . The scalar α in the parametric equation is a fitting constant ($\alpha = 7.718 \mu\text{m}^{-1}$).

E. Contact force (F) versus displacement (u_x) for cylinders with the same height ($H = 100 \mu\text{m}$), thickness ($t = 25 \mu\text{m}$) and elastic modulus ($E = 80 \text{ kPa}$) and varying diameter D , from numerical analyses.

- F. Displacement (u_x) versus time (t) measured in a i3D cylinder incorporated in a chick embryo at different time points in a representative experiment.
- G. Contact force values versus time estimated via the parametric equation using experimental displacement data as input.



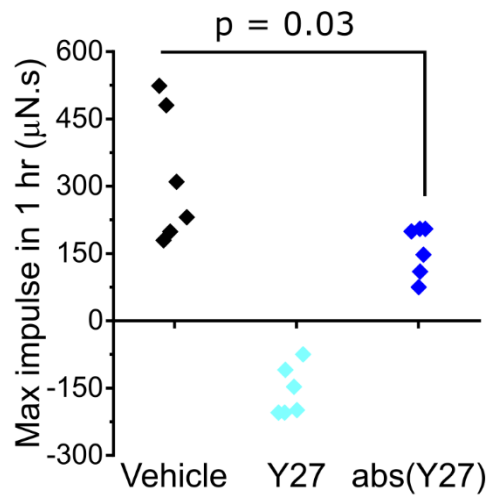
Supplementary Figure 6: i3D cylinder locally resist neuroepithelial bending.

A. 3D reconstruction showing an i3D cylinder suspended between the RNP neural folds. Scale bar 100 μm .

B. Projections showing cylinder deformation over two hours. C and D indicate the positions of the corresponding panels. Scale bar 100 μm .

C-D. Optically-resliced projections showing the curvature of the ventral neuroepithelium (annotated) below the neural fold tips. Dashed lines indicate the T0 contour and the white arrows indicate the change in bending. Scale bar 50 μm .

E. Quantification of the ventral neuroepithelial curvature at the start of imaging and 1.5-2 hours later in seven independent embryos caudal to, or at the level of, the cylinder. P values by T-test paired by embryo.



Supplementary Figure 7: Maximum impulse generated during chick neural fold apposition.

Impulse was calculated as the maximum force applied to the i3D cylinder within 1 hour. Points represent independent embryos. Vehicle embryos are compared against the absolute (non-directional) values of Y27-treated embryos by T-test.

Supplementary References

1. S. C. Chapman, J. Collignon, G. C. Schoenwolf, A. Lumsden, Improved method for chick whole-embryo culture using a filter paper carrier. *Dev Dyn* **220**, 284-289 (2001).
2. J. Schindelin *et al.*, Fiji: an open-source platform for biological-image analysis. *Nat Methods* **9**, 676-682 (2012).

Supplementary Files

This is a list of supplementary files associated with this preprint. Click to download.

- [Supplementarymaterialv13.pdf](#)